JOURNAL OF COMPUTATIONAL PHYSICS 78, 36–63 (1988)

High Resolution Finite Volume Methods on Arbitrary Grids via Wave Propagation

RANDALL J. LEVEQUE*

Mathematics Department, University of Washington,
Seattle, Washington 98195

Received April 30, 1987; revised August 24, 1987

In previous work by the author, a generalization of Godunov's method for systems of conservation laws has been developed and analyzed that can be applied with arbitrary time steps on arbitrary grids in one space dimension. Stability for arbitrary time steps is achieved by allowing waves to propagate through more than one mesh cell in a time step. In this paper the method is extended to second-order accuracy and to a finite volume method in two space dimensions. This latter method is based on solving one-dimensional normal and tangential Riemann problems at cell interfaces and again propagating waves through one or more mesh cells. By avoiding the usual time step restriction of explicit methods, it is possible to use reasonable time steps on irregular grids where the minimum cell area is much smaller than the average cell. Boundary conditions for the Euler equations are discussed and special attention is given to the case of a Cartesian grid cut by an irregular boundary. In this case small grid cells arise only near the boundary, and it is desirable to use a time step appropriate for the regular interior cells. Numerical results in two dimensions show that this can be achieved.

1. INTRODUCTION

Hyperbolic systems of conservation laws in two space dimensions, such as the Euler equations of gas dynamics, have the form

$$u_t + f(u)_x + g(u)_y = 0. \tag{1.1}$$

Here u is a vector of m variables and f and g are the flux functions. In order to solve these equations numerically, the domain is subdivided into computational grid cells (or intervals in one dimension) and an approximation to the solution over each cell is updated in each time step. With traditional explicit methods, the appropriate update is based on cell values in only a few neighboring cells. For example, with a three-point method in one dimension, only the nearest neighbor cells on either side can effect the solution. Most finite volume methods in two space dimensions also limit the domain of dependence to the nearest neighbors.

---

* Supported in part by NSF Grant DMS-8601363 and by the National Aeronautics and Space Administration under NASA Contracts NAS1-17070 and NAS1-18107 while the author was in residence at ICASE, NASA Langley Research Center, Hampton, VA 23665–5225.

0021-9991/88 $3.00

This imposes an obvious limitation on the time step due to the CFL condition, which states that a necessary condition for convergence is that the domain of dependence of the numerical method include the domain of dependence of the true solution, at least in the limit as the grid is refined. For a three-point method in one dimension, this means that the time step k must be restricted by

$$\nu \equiv \frac{k}{h_{\min}} |s_{\max}| \leqslant 1, \tag{1.2}$$

where $h_{\min}$ is the length of the smallest cell and $s_{\max}$ is the maximum wave speed arising in the problem at hand. The quantity ν defined by (1.2) is called the Courant number.

This time step restriction may be reasonable on a uniform grid. An analysis of the truncation error will often show that (1.2) is consistent with the choice of time step required for the temporal accuracy to agree with the spatial accuracy. On the other hand, if the grid is not uniform we would like to replace h_{min} in (1.2) by h_{ave}, some average cell length. If $h_{\min} \ll h_{\text{ave}}$ then (1.2) imposes a severe time step restriction that may greatly reduce the efficiency of the method.

This situation arises, for example, in certain shock tracking procedures (e.g., [16]). In addition to a uniform grid, moving points are introduced that may fall arbitrarily close to the fixed points, creating small cells. Similar difficulties are encountered in the moving mesh method of Harten and Hyman [12], where they must take special care to ensure the proper separation of mesh points.

In more space dimensions, the problem of small mesh cells is difficult to avoid in several common situations. In particular, irregular boundaries cutting through a regular grid (as in Fig. 9.1 and 9.3) result in cells with arbitrarily small area. We would like to choose the time step based on the regular grid cells rather than being artificially restricted by the boundary cells. Small cells are often avoided by using body fitted coordinates, so that the grid cells have more uniform areas. However, this creates additional difficulties in first generating and then computing with the irregular grids. For complicated multicomponent geometries, particularly in three dimensions, the generation of such grids may be very difficult, requiring complicated grid patching. This has led several workers to reconsider the use of Cartesian grids (e.g., [6, 25, 28]).

Similar difficulties arise if a shock is tracked through a fixed grid, at the boundary of a region of mesh refinement or where independent grids are patched together. On general unstructured grids, such as triangulations of arbitrary regions, the cell areas may also vary widely.

In this paper a finite volume method is introduced that avoids these difficulties by dynamically extending the domain of dependence in such a way that the CFL condition is always satisfied. This is accomplished by fully exploiting the wave propagation that is inherent in hyperbolic equations. A one-dimensional Riemann problem is solved normal to each cell interface (meaning the initial data is piecewise constant with a jump discontinuity at the interface). Solving Riemann problems forms the basis of Godunov's classical method and numerous finite volume methods, but in most such methods the Riemann solution is used only to obtain a flux across the boundary. This flux is then used to update only the neighboring cell values.

In the method proposed here, the structure of the Riemann solution is used to a much greater extent. The Riemann solution consists of waves (shocks, contact discontinuities, or rarefaction waves) that propagate away from the interface, each carrying an increment in the flow variables. As a wave propagates, it modifies the flow variables in the cells it passes through. By allowing it to pass through more than one cell, the CFL condition remains satisfied with larger time steps. This gives a generalization of Godunov's method applicable for larger time steps on arbitrary grids. In one space dimension, this first-order accurate method has been developed and analyzed in a series of papers by the author [14–16]. This method is similar in spirit to the "transport collapse" method of Brenier [1–3]. In the present paper, the method is extended to second-order accuracy and arbitrary grids in two space dimensions.

In addition to propagating waves normally from cell interfaces, it is also possible to incorporate tangential wave propagation by solving auxiliary Riemann problems in the orthogonal direction. This leads to increased stability and enhanced modeling of two-dimensional phenomena and propagation of shock waves that are not aligned with the grid.

An additional advantage of the method proposed here is that boundary conditions can be incorporated into the algorithm relatively easily. Farfield nonreflecting boundary conditions and solid wall (or moving piston) boundary conditions for the Euler equations will be discussed here.

The basic idea of the method is described in Section 2 for a scalar equation in one space dimension. A new formulation of the Lax–Wendroff method is presented and then converted to a "high resolution" method (one with sharp nonoscillatory discontinuities and good nonlinear stability properties). The formulation of this method easily allows extension to arbitrary grids and time steps and incorporation of boundary conditions.

In Section 3 the method is extended to systems of conservation laws in one dimension. Boundary conditions for the Euler equations are discussed in Section 4 and then some one-dimensional numerical results are presented in Section 5.

In the remainder of the paper the method is extended to a finite volume method in two dimensions. The special case of a Cartesian grid with irregular boundaries receives particular attention. In Section 9, numerical results are presented for a shock tube problem oblique to the grid and single Mach reflection from a ramp.

2. ONE-DIMENSIONAL SCALAR EQUATIONS

We first consider the one-dimensional scalar conservation law

$$u_t + f(u)_x = 0, \tag{2.1}$$

with $f(u)$ assumed to be a convex function. The computational grid is given by $x_0 < x_1 < \cdots < x_M$. The mesh spacing can be arbitrary and we set $h_i = x_{i+1} - x_i$. The approximate solution on the mesh cell (x_i, x_{i+1}) at time t_n is denoted by U_i^n. The time steps can also be arbitrary and varying. Since the methods are one-step methods and will be described over a single time step, we will denote the current time step simply by $k = t_{n+1} - t_n$ and use the shorthand abbreviations $U_i \equiv U_i^n$ and $\bar{U}_i \equiv U_i^{n+1}$.

For each value of j, set

$$s_j = \begin{cases} (f(U_{j+1}) - f(U_j))/(U_{j+1} - U_j) & \text{if} \quad U_j \neq U_{j+1} \\ f'(U_j) & \text{if} \quad U_j = U_{j+1}. \end{cases} \tag{2.2}$$

Then s_j is the speed at which the discontinuity between U_j and U_{j+1} propagates according to the Rankine–Hugoniot relation. For convenience at this point, suppose that $s_j > 0$ for all j. Then we set

$$u_j(x, t_n) = \begin{cases} U_j & \text{for} \quad x < x_j \\ U_j + (x - x_{j+1/2})\sigma_j & \text{for} \quad x_j \leqslant x < x_{j+1} \\ U_{j+1} & \text{for} \quad x \geqslant x_{j+1}, \end{cases} \tag{2.3a}$$

where $x_{j+1/2} = \frac{1}{2}(x_j + x_{j+1})$ and σ_j is the slope of u_j over the jth interval, as yet unspecified (see Fig. 2.1). Based on these functions, we define an approximate solution $\bar{u}(x, t)$ over the time interval $t_n \leqslant t \leqslant t_{n+1}$. At time t_n, $\bar{u}(x, t_n)$ is simply the piecewise linear function that agrees with $u_j(x, t_n)$ on the jth cell:

$$\bar{u}(x, t_n) = u_j(x, t_n) \qquad \text{for} \quad x_j \leqslant x < x_{j+1}. \tag{2.4a}$$

For $t > t_n$ we let the wave form (2.3a) propagate with speed s_j, defining

$$u_j(x, t) = u_j(x - s_j(t - t_n), t_n). \tag{2.3b}$$

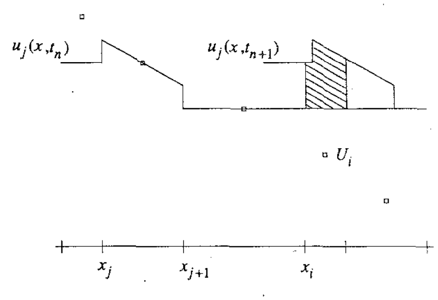

FIG. 2.1. The piecewise linear function u_j at time t_n and after propagation, at time t_{n+1}. Squares indicate the grid values U_{j-1}, U_j, ... The shaded region represents the contribution of this wave toward updating U_i.

These waves are then combined via linear superposition to obtain the approximate solution

$$\bar{u}(x, t) = \bar{u}(x, t_n) + \sum_j (u_j(x, t) - u_j(x, t_n)). \tag{2.4b}$$

The sum in (2.4b) is over all j but at any given point only a finite number of terms will be nonzero since $u_j(x, t_n)$ is constant outside of (x_j, x_{j+1}).

The approximation $\bar{U}_i$ at time t_{n+1} is obtained by projecting the approximate solution $\bar{u}(x, t_{n+1})$ onto the grid, as in Godunov's method (i.e., by averaging over the mesh cell (x_i, x_{i+1})):

$$\begin{aligned}\bar{U}_i &= \frac{1}{h_i}\int_{x_i}^{x_{i+1}} \bar{u}(x, t_{n+1})\, dx \\ &= U_i + \frac{1}{h_i}\sum_j \int_{x_i}^{x_{i+1}} (u_j(x, t_{n+1}) - u_j(x, t_n))\, dx.\end{aligned} \tag{2.5}$$

Note that $\bar{U}_i$ is obtained from U_i by adding to it contributions from several neighboring cells. Figure 2.1 shows the typical contribution to U_i, indicated by the shaded area.

For a linear problem $u_t + su_x = 0$ with constant speed s, the approximation $\bar{u}(x, t)$ is in fact the true solution with initial data $\bar{u}(x, t_n)$. For nonlinear problems the waveform (2.3a) should be distorted for $t > t_n$, and so (2.3b) represents a local linearization of the flux function. The superposition (2.4b) is a further linearization of the nonlinear problem. In spite of this, it is possible to achieve second-order accuracy with appropriate choices of σ_j.

There are various ways to specify the slope σ_j. Three possibilities are

$$\sigma_j^{\mathrm{G}} = 0 \qquad \text{(Godunov)} \tag{2.6a}$$

$$\sigma_j^{\mathrm{LW}} = (U_{j+1} - U_j)/(x_{j+3/2} - x_{j+1/2}) \qquad \text{(Lax–Wendroff)} \tag{2.6b}$$

$$\sigma_j^{\mathrm{M}} = \operatorname{minmod}(\sigma_j^{\mathrm{LW}}, \sigma_{j-1}^{\mathrm{LW}}) \qquad \text{(minmod)}, \tag{2.6c}$$

where the minmod function is defined by

$$\operatorname{minmod}(a, b) = \tfrac{1}{2}(\operatorname{sgn}(a) + \operatorname{sgn}(b)) \min(|a|, |b|).$$

The names assigned to the first two choices of σ are based on the fact that the method reduces to one of these standard methods on a uniform grid with Courant number $\nu < 1$. Then each U_i is influenced by at most two waves and the method can be rewritten as a three-point scheme. Setting $\nu_i = s_i k/h$ and computing the integrals in (2.5) explicitly, we obtain (still assuming $s_j > 0$ for all j)

$$\bar{U}_i = U_i - \nu_{i-1}(U_i - U_{i-1}) + \tfrac{1}{2}\nu_{i-1}(1 - \nu_{i-1})\,\sigma_{i-1}h - \tfrac{1}{2}\nu_i(1 - \nu_i)\,\sigma_i h. \tag{2.7}$$

This can be rewritten in conservation form as

$$\bar{U}_i = U_i - \frac{k}{h}(F_i - F_{i-1}), \tag{2.8}$$

where

$$F_j = f(U_j) + \tfrac{1}{2}(1 - v_j)\, s_j \sigma_j h. \tag{2.9}$$

If $\sigma_j \equiv 0$ this gives the first-order upwind scheme, which agrees with Godunov's method for the problem considered here. With slope (2.6b), this is easily seen to be the standard Lax–Wendroff method.

The Lax–Wendroff method is second-order accurate on smooth solutions, but it generally develops oscillations and possibly instabilities near discontinuities or sharp gradients. The minmod choice of slopes (2.6c) is designed to avoid this difficulty. Van Leer [27] used a similar geometric approach with limited slopes to define his second-order accurate MUSCL schemes. Later Goodman and Le Veque [10, 18] used the minmod slope (2.6c) to derive a total variation diminishing (TVD) version of van Leer's method. The method (2.7) with this choice of σ is closely related to these methods and to a variety of other "high resolution" schemes that have recently been proposed (e.g., [11, 19, 20, 29]). In particular, for a linear problem with $f(u) = au$ and $a > 0$, (2.7) with minmod slopes is precisely the minmod flux-limiter method introduced by Roe (see Sweby [26]) and hence is TVD.

It is interesting to note that the minmod method proposed here is not TVD on nonlinear problems. It is possible to produce examples where the variation increases slightly, although detrimental oscillations or instabilities have never been observed. Indeed, the lack of TVD may be an advantage since any TVD method must reduce to first order accuracy at extreme points [19]. In numerical experiments, the present method appears to perform better at such points.

The main advantage of this approach, however, is that we can easily go beyond formula (2.7) and apply the method as described by (2.5) with arbitrary grids and time steps.

Before discussing systems of conservation laws, we point out a slightly different formulation of the method that helps simplify its implementation and extension to two space dimensions. We can decouple the wave propagation into a two stage procedure. In the first stage we propagate the wave $u_j^{(1)}(x, t)$ given by (2.3) with $\sigma_j = 0$, corresponding to the first-order algorithm. In the second stage we propagate a second-order correction wave,

$$u_j^{(2)}(x, t) = u_j(x, t) - u_j^{(1)}(x, t),$$

with the same speed s_j. This wave has integral zero and initially has the form

$$u_j^{(2)}(x, t_n) = \begin{cases} (x - x_{j+1/2})\sigma_j & \text{for } \; x_j \leqslant x < x_{j+1} \\ 0 & \text{otherwise.} \end{cases}$$

When viewed in this way it is clear how the second-order correction relates to the flux corrected transport (FCT) algorithm of Boris and Book [3] and Zalesak [30] and to the ideas of Roe [22]. The results of the first-order accurate scheme are corrected by redistributing some of the flux between grid cells.

In the above discussion we assumed that $s_j > 0$. If $s_j < 0$ we must replace (2.3) by

$$u_j(x, t_n) = \begin{cases} U_j & \text{for} \quad x < x_{j+1} \\ U_j + (x - x_{j+3/2})\sigma_j & \text{for} \quad x_{j+1} \leqslant x < x_{j+2} \\ U_{j+1} & \text{for} \quad x \geqslant x_{j+2} \end{cases} \tag{2.10}$$

in order to obtain a method that reduces to the Lax–Wendroff or minmod method in the special cases described above. In the latter case we also redefine

$$\sigma_j^{\mathrm{M}} = \mathrm{minmod}(\sigma_j^{\mathrm{LW}}, \sigma_{j+1}^{\mathrm{LW}}).$$

Note that the linear segment in $u_j(x, t)$ is always behind the discontinuity as it propagates.

3. Systems of Conservation Laws in One Dimension

We now develop the method more generally for hyperbolic systems of conservation laws (2.1) with $u \in \mathbb{R}^m$. We assume that the Jacobian matrix $f'(u)$ has real eigenvalues $\lambda_j(u)$ for all u and that each characteristic field is either genuinely nonlinear or linearly degenerate. Then the Riemann problem, consisting of (2.1) with piecewise constant initial conditions

$$u(x, t_n) = \begin{cases} U_j & x < x_{j+1} \\ U_{j+1} & x \geqslant x_{j+1} \end{cases} \tag{3.1}$$

has a solution for $\| U_{j+1} - U_j \|$ sufficiently small. This similarity solution consists of $m+1$ constant states separated by shocks, contact discontinuities, or rarefaction waves. (See Lax [13] for a description of the theory.)

Although the method can be adapted to use this exact Riemann solution, we will base the method on an approximate Riemann solution of the type introduced by Roe [21]. The Riemann solution of (2.1) with data (3.1) is replaced by the solution of the linear problem

$$u_t + A_j u_x = 0, \tag{3.2}$$

where $A_j = A_j(U_j, U_{j+1})$ is an appropriate average value of $f'(u)$. This gives a good approximation, particularly for smooth solutions where $\| U_{j+1} - U_j \| = O(h)$. Denote the solution of this problem by $u_j^{(1)}(x, t)$ for $t \geqslant t_n$. Then $u_j^{(1)}(x, t)$ consists of $m+1$ constant states separated by discontinuities travelling with speeds

$$s_{j1} \leqslant s_{j2} \leqslant \cdots \leqslant s_{jm} \tag{3.3}$$

which are eigenvalues of A_j. The jump in $u_j^{(1)}$ across the pth such wave is an eigenvector R_{jp} of A_j, so that

$$A_j R_{jp} = s_{jp} R_{jp} \tag{3.4}$$

and $U_{j+1} - U_j$ is decomposed as

$$U_{j+1} - U_j = \sum_{p=1}^{m} R_{jp}. \tag{3.5}$$

To obtain high resolution we will also introduce a correction wave $u_j^{(2)}(x, t)$ by generalizing the scalar case discussed in Section 2. We break $u_j^{(2)}$ up into m correction waves $u_{jp}^{(2)}$, $p = 1, 2, ..., m$ each of which travels with speed s_{jp} and has an initial form that is piecewise linear and nonzero over a single mesh interval. The choice of interval again depends on the sign of s_{jp}: For $s_{jp} > 0$:

$$u_{jp}^{(2)}(x, t_n) = \begin{cases} (x - x_{j+1/2})\sigma_{jp} & \text{for} \quad x_j \leqslant x < x_{j+1} \\ 0 & \text{otherwise.} \end{cases} \tag{3.6a}$$

For $s_{jp} \leqslant 0$:

$$u_{jp}^{(2)}(x, t_n) = \begin{cases} (x - x_{j+3/2})\sigma_{jp} & \text{for} \quad x_{j+1} \leqslant x < x_{j+2} \\ 0 & \text{otherwise,} \end{cases} \tag{3.6b}$$

where σ_{jp} is now a slope vector with m components, to be defined below. We now set

$$u_j^{(2)}(x, t) = \sum_{p=1}^{m} u_{jp}^{(2)}(x, t) = \sum_{p=1}^{m} u_{jp}^{(2)}(x - s_{jp}(t - t_n), t_n) \tag{3.7}$$

and

$$u_j(x, t) = u_j^{(1)}(x, t) + u_j^{(2)}(x, t). \tag{3.8}$$

Based on these functions $u_j(x, t)$, we can define an approximate solution $\bar{u}(x, t)$ just as in the scalar case via (2.4). Averaging $\bar{u}(x, t_{n+1})$ over the ith interval as in (2.5) gives the numerical solution $\bar{U}_i$ at time t_{n+1}.

If $\sigma_{jp} \equiv 0$ then $u_j^{(2)}(x, t) \equiv 0$ for all j. In this case the method reduces to the large time step generalization of Godunov's method (with Roe's approximate Riemann solver) that has been previously studied [14–16]. This method is conservative for any mesh ratio as is shown in [14] where the method is rewritten in conservation form. Note that the method remains conservative with arbitrary slope vectors since $\int_{-\infty}^{\infty} u_j^{(2)}(x, t)\, dx = 0$ for any σ_{jp}. We can view the function $u_j(x, t)$ for $t \geqslant t_n$ as a new approximate Riemann solver which gives second-order accuracy for an appropriate choice of σ_{jp}. Because of this the high resolution method with nonzero σ_{jp} can also be written in conservation form following Section 4 of [14].

Corresponding to the three slope choices (2.6), we now have

$$\sigma_{jp}^{\mathrm{G}} = 0 \qquad \text{(Godunov–Roe)}, \tag{3.9a}$$

$$\sigma_{jp}^{\mathrm{LW}} = R_{jp}/(x_{j+3/2} - x_{j+1/2}) \qquad \text{(Lax–Wendroff)}, \tag{3.9b}$$

$$\sigma_{jp}^{\mathrm{M}} = \operatorname{minmod}(\sigma_{jp}^{\mathrm{LW}}, \sigma_{Jp}^{\mathrm{LW}}) \qquad \text{(minmod)}, \tag{3.9c}$$

where in (3.9c) $J = j - \operatorname{sgn}(s_{jp})$ and the minmod function is applied to vectors componentwise. Either of the last two choices appears to give second-order accuracy on smooth solutions. In order to achieve stability and nonoscillatory behavior near discontinuities, the minmod slope (3.9c) is recommended and has been used in the numerical experiments reported below.

This method appears difficult to implement from the description just given. In fact, it is quite simple if we consider each wave arising from each Riemann problem in turn and compute its effect on the solution. Due to the linearization of wave interactions that is used here, each wave can be propagated and averaged onto the grid independently of all other waves. For the case $\sigma_{jp} \equiv 0$ this algorithm has already been described in some detail in [15, 16]. This gives propagation of the waves $u_{jp}^{(1)}$.

The correction waves $u_{jp}^{(2)}$ simply give a redistribution between mesh cells. In particular, if the mesh is uniform, then the nonzero portion of $u_{jp}^{(2)}$ overlaps at most two cells, independent of the Courant number, and the second-order correction is easily implemented.

For linear systems of equations, solution of the Riemann problems gives resolution into the characteristic variables and $\bar{u}(x, t)$ is again the exact solution with the piecewise linear data $\bar{u}(x, t_n)$, for all $t \geqslant t_n$. Consequently, the method gives second-order accuracy with any size time step in this case. For nonlinear problems with smooth solutions, the superposition (2.4) can be shown to be consistent with second-order accuracy. Towards this end, a semidiscrete version of this superposition (discretized only in time) is investigated in [17] and shown to produce an approximate solution with $O(k^3)$ error over a time step of length k.

4. BOUNDARY CONDITIONS FOR THE EULER EQUATIONS

One advantage of the approach used here is the ease with which boundary conditions can be derived and implemented, based on the physics of the problem. This will be illustrated for the Euler equations at a free field (non-reflecting) boundary and at a solid wall (or moving piston) boundary.

The Euler equations of gas dynamics have the form

$$\begin{pmatrix} \rho \\ \rho v \\ E \end{pmatrix} + \begin{pmatrix} \rho v \\ \rho v^2 + p \\ (E+p)v \end{pmatrix} = 0, \tag{4.1}$$

where ρ, v, p, and E represent the density, velocity, pressure, and energy, respectively. These quantities are related by $E = p/(\gamma - 1) + \frac{1}{2}\rho v^2$ with $\gamma = 1.4$ for air.

Non-reflecting boundary conditions are easily achieved by simply allowing all waves which cross the boundary to pass out of the region, with no incoming waves. In a subsonic problem these boundary conditions are not strictly correct. For example, if two shocks propagate out of the domain at different times, they may interact (in the exterior) and give rise to a weak rarefaction wave which should reenter the domain at a later time. Correctly modeling such behavior requires boundary conditions which are nonlocal in time. Simply letting the waves pass out appears to be the best that can be achieved with local boundary conditions and is easily implemented with arbitrary grids and time steps.

At a solid wall boundary the correct boundary condition is $v = 0$. This gives rise to a boundary Riemann problem which can be solved for the incoming wave. Note that the boundary is characteristic in this case, so that there is only one incoming wave.

Another way to impose this boundary condition for the PDE is to extend the domain beyond the boundary and specify initial conditions obtained by suitably reflecting the values from the interior. For example, if we wish to compute over time k and $s_{\max}$ represents the maximum wave speed, then it suffices to extend the domain from $x = 0$, say, to $x^* = -ks_{\max}$ and set

$$\begin{aligned} \rho(x) &= \rho(-x) \\ v(x) &= -v(-x) \\ p(x) &= p(-x) \end{aligned} \tag{4.2}$$

for $x^* \leqslant x \leqslant 0$. Solving the problem over this extended domain (using, for example, non-reflecting boundary conditions at $x = x^*$), will give the desired solution for $x \geqslant 0$ with the boundary condition $v(0, t) = 0$ satisfied.

This latter approach is easy to implement numerically on arbitrary grids. New grid points are introduced exterior to the original domain by reflecting the interior points which fall within distance $ks_{\max}$ of the boundary. The values on these mesh cells are obtained by reflecting the interior values as in (4.2). Then any wave leaving the original domain during the timestep is matched by a "reflected" wave which enters at the same point in time. The jump in v in the entering wave is the negative of the jump in v in the exiting wave (due to the symmetry in solutions to the Riemann problem under the reflection (4.2)) and hence the boundary condition is always satisfied. This same symmetry exists in Roe's approximate Riemann solver and the slopes σ_{jp} will also be symmetric, so that the boundary condition remains satisfied for the method discussed here. Again the procedure is easily implemented for arbitrary time steps and meshes. Finally, it is clear that the method has the same order of accuracy near the boundary as in the interior, since after the reflection the boundary essentially disappears and we are simply using the interior scheme everywhere.

If the solid wall boundary is moving (as, for example, in a piston problem), then boundary conditions are also easily derived. If the piston is located at $x = z_n$ at time t_n and is moving with speed s_0 (assumed constant) for $t_n \leqslant t \leqslant t_{n+1}$, then the mesh cells for $z_n \leqslant x \leqslant z_n + s_{\max} k$ are reflected to the left of z_n with grid values

$$\begin{aligned} \rho(z_n - x) &= \rho(z_n + x) \\ v(z_n - x) &= 2s_0 - v(z_n + x) \\ p(z_n - x) &= p(z_n + x). \end{aligned} \tag{4.3}$$

The waves generated from these cell boundaries will interact with the interior waves in such a way that $v(z_n + s_0(t - t_n), t) = s_0$ will be satisfied for $t_n \leqslant t \leqslant t_{n+1}$.

5. NUMERICAL RESULTS IN ONE DIMENSION

On a uniform grid with $\nu < 1$ the present minmod method performs much like the minmod flux limiter method discussed by Sweby [26]. Figure 5.1 shows some results for a shock tube problem with the Euler equations and initial data with

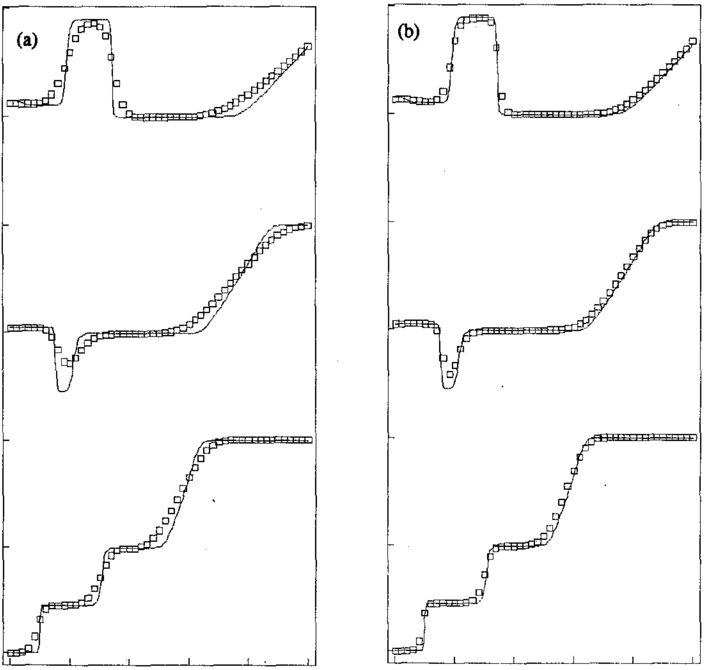

FIG. 5.1. The density ρ in the shock tube problem at three different times (reading upward). Figure (a) shows the values obtained with slopes $\sigma_{jp} = 0$. Figure (b) shows the values obtained with minmod slopes (3.9c).

$v=0$ everywhere and $\rho=p=1$ for $x<0.4$, $\rho=p=3$ for $x>0.4$. The solution at three different times is shown. Note that the shock reflects off a solid wall boundary at $x=0$ and then interacts with the contact discontinuity. Nonreflecting boundary conditions were used at $x=1$, where the rarefaction wave begins to leave the region.

Figure 5.1a shows the density ρ computed using the first-order accurate method with Godunov slopes $\sigma_{jp}=0$. Figure 5.1b shows the results with minmod slopes. In each case $h=0.02$ and $k=h/2$ corresponding to $\nu \cong 0.75$. The solid line in each figure is the solution computed with 201 mesh points using minmod slopes.

Figure 5.2 demonstrates the ability of this method to deal with nonuniform meshes. In this problem smooth initial conditions were specified:

$$\rho(x,0)=1.0+0.1\cos(2.5x), \quad v(x,0)=0.1\sin(5x), \quad p(x,0)=1.8+0.1\cos(2.5x),$$

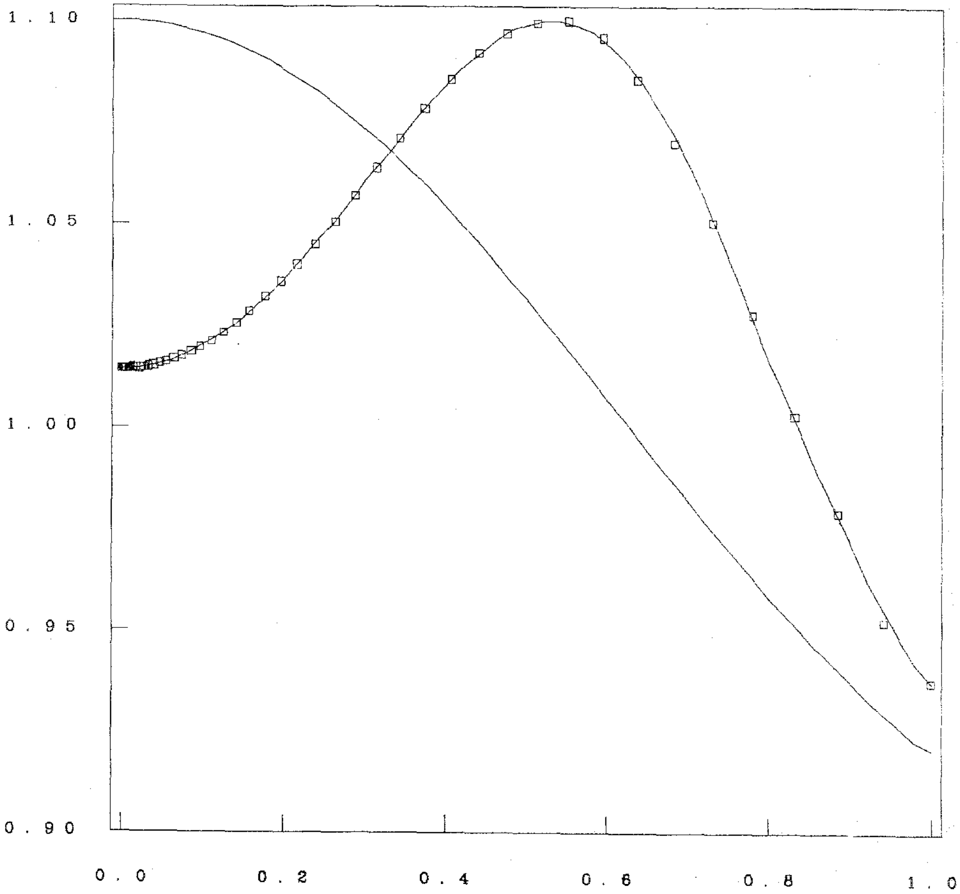

FIG. 5.2. Density in a smooth solution computed on a uniform grid (solid line) and on nonuniform grid (squares) with Courant number 2500. The initial conditions $\rho(x,0)$ are also shown.

again with a solid wall boundary at $x=0$ and nonreflecting boundary conditions at $x=1$. The solid line shows the resulting density at $t=0.1$ computed with 51 equally spaced mesh points and $k=h=0.02$, giving $\nu \cong 1$. The squares show the solution computed with 51 mesh points $x_j=((j-1)h)^3$ densely clustered near $x=0$. Again $k=0.02$ but now the Courant number, based on the smallest mesh width h_1, is roughly 2500. The numerical solution does not appear to be adversely affected by this.

6. Finite Volume Methods in Two Dimensions

In two space dimensions, the wave propagation approach can be used to rewrite a standard finite volume method in a way that can be easily extended to allow larger timesteps than are normally possible. As noted in the Introduction, this might be valuable with nonuniform grids where some of the grid cells are considerably smaller than average. Standard explicit methods have a stability restriction that limits the time step in terms of the smallest cell area. Of particular interest is a uniform Cartesian grid in which some of the grid cells are cut off by an irregular boundary, a tracked shock, or an area of mesh refinement. To some extent the discussion will be specialized to this situation, but the ideas can be applied on more general unstructured grids as well.

In one space dimension, we have seen that nonuniform grid cells are easily handled by allowing waves to propagate entirely through a small cell and out the other side. The same approach can be taken in two dimensions with waves arising at cell interfaces. The basic algorithm will be described on a general unstructured grid.

Associated with each grid cell C_j is an approximation U_j to the solution $u(x, y, t_n)$ over this grid cell. We also define A_j to be the area of C_j and h_{ij} to be the length of the face separating adjacent cells C_i and C_j. We begin by describing a Godunov-type scheme and will later introduce high resolution corrections based on piecewise linear approximations.

In a finite volume method, fluxes across the cell faces are defined and used to update the cell values on either side of the face. Consider, for example, the face separating C_i and C_j in Fig. 6.1. A flux can be defined by solving a one-dimensional Riemann problem normal to the face. Define new variables ξ (normal to the face) and η (tangential) by

$$\xi=\alpha x+\beta y, \qquad \eta=-\beta x+\alpha y \tag{6.1}$$

with $\alpha=\cos\theta$, $\beta=\sin\theta$, where θ is the angle of the cell interface. The conservation laws

$$u_t+f(u)_x+g(u)_y=0 \tag{6.2}$$

are transformed to

$$u_t+F(u)_\xi+G(u)_\eta=0, \tag{6.3}$$

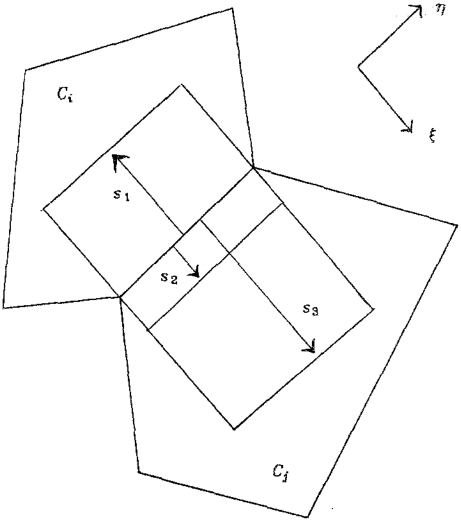

FIG. 6.1. Two grid cells C_i and C_j from an unstructured grid. Wave propagation from the cell interface is determined by solving a one dimensional Riemann problem in the ξ-direction, giving rise to waves propagating with velocities s_1, s_2, and s_3.

where

$$\begin{aligned} F(u) &= \alpha f(u) + \beta g(u) \\ G(u) &= -\beta f(u) + \alpha g(u). \end{aligned} \tag{6.4}$$

In the new coordinates u is constant in η and so (6.3) reduces to a one-dimensional Riemann problem

$$u_t + F(u)_\xi = 0 \tag{6.5}$$

with left and right states U_i and U_j. For rotationally invariant equations such as the Euler equations this is particularly simple since, after a change of dependent variables to rotate the velocity field, the form of $F(u)$ agrees with $f(u)$ and hence a single Riemann solver suffices for all angles θ.

As in the one-dimensional algorithm, we use Roe's approximate Riemann solver and obtain a set of waves traveling with speeds $s_1, s_2, ..., s_m$ in the ξ-direction. As before we denote the jumps in u across these waves by the vectors $R_1, ..., R_m$, so that

$$U_j - U_i = \sum_p R_p. \tag{6.6}$$

Figure 6.1 shows these waves propagating from the interface in a situation where the waves lie entirely within neighboring cells.

We think of u being incremented by $-\operatorname{sgn}(s_p)R_p$ at each point swept out by the pth wave. Consequently, the average value U_i of u over the cell C_i in Fig. 6.1, for example, will be incremented by

$$\left(\frac{|s_1|\,kh_{ij}}{A_i}\right)R_1. \tag{6.7}$$

The factor multiplying R_1 is the ratio of the area swept out by the 1-wave to the total cell area. Similarly, U_j is incremented by

$$\left(\frac{s_2kh_{ij}}{A_j}\right)(-R_2)+\left(\frac{s_3kh_{ij}}{A_j}\right)(-R_3). \tag{6.8}$$

These increments to U_i and U_j can be interpreted more traditionally in terms of a flux-difference splitting. The total increment to u (which has been split between C_i and C_j and averaged over these cells) is the sum of A_i times (6.7) plus A_j times (6.8), giving

$$-kh_{ij}[s_1R_1+s_2R_2+s_3R_3]. \tag{6.9}$$

A basic property that Roe's approximate Riemann solver shares with the exact Riemann solution is that

$$\sum s_pR_p=F(U_j)-F(U_i) \tag{6.10}$$

so that (6.9) becomes

$$-kh_{ij}(F(U_j)-F(U_i)). \tag{6.11}$$

This is the flux difference between C_i and C_j which has been split via (6.7) and (6.8).

The method as described so far is thus equivalent to traditional flux-difference splitting methods. By integrating the conservation laws around each cell, it is easily shown that such methods are conservative for any splitting of the flux difference. A variety of such methods have been proposed, most of which share the property that flux differences are split only between C_i and C_j with no contribution to other cells. This leads to a restriction on the time step, since clearly the factor multiplying R_1 in (6.7), for example, should be no greater than 1 for stability. If A_i is very small, this gives a severe restriction on k.

The advantage of the wave propagation interpretation of Fig. 6.1 is twofold. First, it makes it clear that in some circumstances other cells should also be affected. More importantly, it makes it easy to determine exactly what that effect should be. Figure 6.2 shows a typical wave propagating over a different grid. Each cell value should clearly be updated by $\operatorname{sgn}(s_p)R_p$ times the ratio of the shaded area within the cell to the total cell area. Note that this ratio is always less than or equal to 1. Splitting each wave in this manner and adding up all increments to all cells

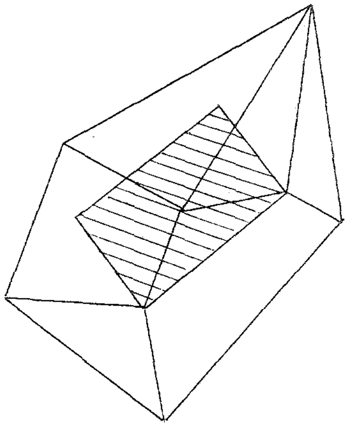

FIG. 6.2. Propagation of a wave over a general unstructured grid. Cell values are updated in every cell the wave intersects. The contribution to each cell is proportional to the ratio of the shaded area within that cell to the total cell area.

gives the same total increment (6.9) and hence the method remains conservative, while being much more stable in a situation such as Figure 6.2 than a method that increments only C_i and C_j.

Instabilities can still arise, however, as illustrated by the following simple example. Consider the scalar linear advection equation

$$u_t + u_x + u_y = 0 \tag{6.12}$$

on a uniform rectangular mesh with initial data consisting of a sawtooth discontinuity at 45° to the mesh:

$$U_{ij} = \begin{cases} 1 & \text{if } i+j \leqslant M \\ 0 & \text{if } i+j \geqslant M+1 \end{cases}$$

for some M. If $k \leqslant h/2$ then the method described above is stable and in fact for $k = h/2$ gives the exact solution, a wave propagating through one additional diagonal of mesh cells in each time step:

$$\bar{U}_{ij} = \begin{cases} 1 & \text{if } i+j \leqslant M+1 \\ 0 & \text{if } i+j \geqslant M+2. \end{cases}$$

For larger k, however, the method is unstable. For example, if $k = h$ then the wave should propagate through two additional diagonals in each step. Instead the waves propagating in the x- and y-directions overlap and give the value $\bar{U}_{ij} = 2$ for $i + j = M + 1$ with no propagation into the second diagonal. In later time steps this instability grows exponentially.

In order to avoid this difficulty, it appears to be necessary to include tangential wave propagation as well as normal propagation. For Eq. (6.12) it is easy to see how to include tangential propagation. All waves should propagate with tangential

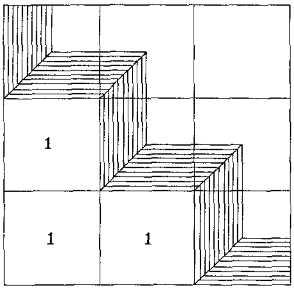

FIG. 6.3. Wave propagation for the scalar problem (6.12) when tangential wave propagation is included. Shown for a time step $k=h/2$.

velocity 1 as well as normal velocity 1. Figure 6.3 shows this wave propagation in the case $k=h/2$, giving

$$\bar{U}_{ij}=\begin{cases} 1 & \text{if } i+j<M+1 \\ 0.75 & \text{if } i+j=M+1 \\ 0.25 & \text{if } i+j=M+2 \\ 0 & \text{if } i+j>M+2 \end{cases}.$$

The method now gives exact propagation with $k=h$ and indeed, except for smearing introduced by the averaging process, this modified method gives exact propagaton for any time step k.

For nonlinear systems of equations the tangential propagation is introduced as follows. After solving the normal Riemann problem we have waves R_p traveling with speeds s_p normal to the cell face. Suppose now that we split up the wave R_p into subwaves $R_p^{(1)}, R_p^{(2)}, \ldots, R_p^{(m)}$ with

$$\sum_{q=1}^{m} R_p^{(q)}=R_p \tag{6.13}$$

and assign tangential velocities $s_p^{(1)}, \ldots, s_p^{(m)}$. The wave in Figure 6.2, for example, might be split into two waves $R_p^{(1)}$ and $R_p^{(2)}$ with tangential speeds $s_p^{(1)}$ and $s_p^{(2)}$ as shown in Fig. 6.4. Note that the area swept out by each wave is $|s_p|\,kh_{ij}$, the same as the area of the original wave in Fig. 6.2, independent of the tangential speeds $s_p^{(q)}$. If each of these waves is propagated as before to increment neighboring mesh cells, the total increment will be

$$-kh_{ij}[s_pR_p^{(1)}+s_pR_p^{(2)}]=-kh_{ij}s_pR_p \tag{6.14}$$

in view of (6.13). Hence the method remains conservative for an arbitrary splitting $R_p^{(q)}$ and arbitrary speeds $s_p^{(q)}$ provided only that (6.13) is satisfied.

A natural way to choose the splitting is by solving a tangential Riemann problem with initial data having a discontinuity of magnitude R_p. For the equation we take the tangential portion of (6.3),

$$u_t+G(u)_\eta=0. \tag{6.15}$$

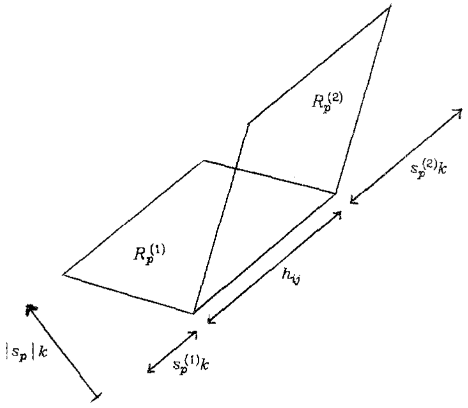

FIG. 6.4. The wave R^p is split tangentially into two waves $R_p^{(1)}$ and $R_p^{(2)}$ with tangential speeds $s_p^{(1)}$ and $s_p^{(2)}$.

Figure 6.1 suggests a possible set of initial data. The wave R_p propagates with the state

$$U_i + \sum_{q<p} R_q \tag{6.16a}$$

to one side and

$$U_j - \sum_{q>p} R_q \tag{6.16b}$$

to the other. Taking these as the left and right states for Eq. (6.15) gives a discontinuity of magnitude R_p which will then be resolved into waves $R_p^{(1)}, ..., R_p^{(m)}$ propagating in the η direction with speeds $s_p^{(1)}, ..., s_p^{(m)}$.

For the linear equation (6.12), $m = 1$, $s_1 = 1$, and $s_1^{(1)} = 1$ for all i, j. This gives the correct propagation as described above. More generally, consider a linear system

$$u_t + Au_x + Bu_y = 0.$$

First suppose that A and B have identical eigenvectors and hence are simultaneously diagonalizable. Then each wave R_p obtained by splitting $U_j - U_i$ into eigenvectors of A is already an eigenvector of B as well, so that $R_p^{(p)} = R_p$ and $R_p^{(q)} = 0$ for $q \neq p$. The normal and tangential speeds s_p and $s_p^{(p)}$ are the corresponding eigenvalues of A and B, respectively. In this case the method gives exact propagation (followed by smearing due to the averaging process) for any time step k and we are essentially using the method of characteristics.

If A and B are not simultaneously diagonalizable, or for nonlinear systems, each wave R_p will in general be split into m waves $R_p^{(q)}$. Except in special circumstances the method will not give exact propagation and the time step will need to be restricted in order to obtain reasonable results. Also note that when waves from different interfaces overlap, they are combined by linear superposition as in the one-dimensional algorithm. This incurs additional errors on nonlinear problems. A serious error analysis of the method has not yet been attempted, but the numerical results of Section 9 give some indication of its capabilities.

In the special case of a uniform Cartesian grid, with $h_{ij} \equiv h$ and $A_i \equiv h^2$, the wave propagation becomes relatively simple, particularly if the Courant number $kh\,|s_{\max}|/h^2$ is less than 1. Then each wave affects at most two cells, as in Figure 6.3, and the areas of intersection are easy to compute. Although we do not present the details, the method can be written as a nine-point finite difference method in conservation form. If tangential wave propagation is suppressed, the method reduces to a five-point scheme.

7. HIGH RESOLUTION IN TWO DIMENSIONS

Greater accuracy for smooth flows and better resolution of discontinuities can be obtained by introducing piecewise linear approximations as in the one-dimensional method. Ideally one might like to use bilinear approximations matching slopes in the x- and y-directions simultaneously, but it turns out that a simpler approach is sufficient to reproduce the Lax–Wendroff method for scalar problems on uniform grids. Introducing minmod slope limiting gives a stable second-order correction that is easy to generalize and implement for nonlinear systems on arbitrary grids.

First consider a uniform Cartesian grid with Courant number less than one and suppress tangential propagation. Then we obtain a five-point flux-splitting method as discussed above. We can think of implementing this by applying the first-order one-dimensional algorithm of Section 3 simultaneously in the x- and y-directions. It is natural then to also apply the second-order correction wave introduced there. In handling the interface between U_{ij} and $U_{i+1,j}$, for example, we obtain waves [illegible]

$$-\left(\frac{s_p k}{h}\right) R_p$$

according to the first-order algorithm. For the second-order correction we propagate the wave $u^{(2)}$ from Section 3, viewed now as a two-dimensional wave that is constant in y over the grid cells in question and piecewise linear in x. Thus $U_{i+1,j}$ is incremented by $\frac{1}{2}(k/h)\,s_p(h-ks_p)\sigma_p$ while U_{ij} is incremented by $-\frac{1}{2}(k/h)\,s_p(h-ks_p)\sigma_p$, where σ_p is the slope vector in the x-direction, again defined by one of (3.9). Wave propagation in the y-direction is handled in an analogous manner.

If we choose the Lax–Wendroff slope (3.9b), $\sigma_p = R_p/h$, then for scalar equations the method just described reduces to the following:

$$\begin{aligned} U_{ij}^{n+1} = U_{ij} - \frac{k}{2h}\,[f(U_{i+1,j}) - f(U_{i-1,j}) + g(U_{i,j+1}) - g(U_{i,j-1})] \\ + \frac{k^2}{2h^2}\left[\frac{(f(U_{i+1,j}) - f(U_{ij}))^2}{U_{i+1,j} - U_{ij}} - \frac{(f(U_{ij}) - f(U_{i-1,j}))^2}{U_{ij} - U_{i-1,j}}\right. \\ \left. + \frac{(g(U_{i,j+1}) - g(U_{ij}))^2}{U_{i,j+1} - U_{ij}} + \frac{(g(U_{ij}) - g(U_{i,j-1}))^2}{U_{ij} - U_{i,j-1}}\right]. \end{aligned} \tag{7.1}$$

This method is not second-order accurate as it stands, since it is missing the cross derivative terms $\frac{1}{2}k^2[(f'(u)\,g(u)_y)_x + (g'(u)\,f(u)_x)_y]$ that arise in a Taylor series expansion of $u(x_i, y_j, t_{n+1})$. Remarkably, if we now introduce tangential propagation of the first order waves, the algorithm is modified by terms modeling these cross derivatives and second order accuracy is achieved. The modification is one-sided and the exact form depends on the signs of $f'(u)$ and $g'(u)$.

Note that the second order correction waves are **not** split tangentially. Consequently, on uniform grids the second-order correction is very easy to implement and adds little cost to the algorithm. In practice the method is modified by using minmod slopes (3.9c) to eliminate oscillations while retaining second order accuracy on smooth flows.

On unstructured grids, a high resolution correction can be defined in various ways. Here is one untested possibility, motivated by the above treatment of uniform grids. Let ξ and η be the local coordinate directions defined by the interface between C_i and C_j. For the pth wave, define a slope vector σ_p in the ξ-direction (normal to the interface). The simplest choice would be the "Lax–Wendroff" slope

$$\sigma_p = R_p/h^*, \tag{7.2}$$

where h^* is some measure of the normal distance between cells C_i and C_j, such as the difference in ξ-coordinates of the centers of mass of these two cells. Then a piecewise linear wave with this slope in the ξ-direction, zero slope in the η-direction, and total integral zero can be propagated in the ξ-direction with velocity s_p. The shape of the region where the slope is σ_p is still undetermined. Following the one-dimensional method, we could choose the region to be the cell C_i if $s_p > 0$ and C_j if $s_p < 0$. To be specific, assume that $s_p > 0$ and let (ξ_c, η_c) be the center of mass of the cell C_i, in the local coordinates determined by the interface. Then the high resolution correction, which must be averaged onto the cells, is the piecewise linear function

$$u^{(2)}(\xi, \eta, t_{n+1}) = \begin{cases} (\xi - s_p k - \xi_c)\sigma_p & \text{if } (\xi - s_p k, \eta) \in C_i \\ 0 & \text{otherwise.} \end{cases}$$

In problems with shocks one would again like to introduce a slope limiter instead of using (7.2) directly. The best way to do this on unstructured grids has not yet been determined.

8. Boundary Conditions in Two Dimensions

Nonreflecting outflow boundary conditions are implemented in two dimensions in exactly the same way as in one dimension. Waves propagating out of the computational domain at such a boundary simply disappear and no new waves are propagated inward from boundary interfaces.

At a solid wall boundary, the proper boundary conditions for the Euler equations are obtained by specifying zero normal velocity. If the boundary is flat, this boundary condition can be implemented in the same way as was done in Section 4 for the one-dimensional Euler equations. We will consider this simple case first and see how to reinterpret it in a manner more suited to arbitrary boundaries. For flat boundaries, the grid cells near the boundary can be reflected across the boundary to form fictitious cells as in Fig. 8.1. We assign values of U in these exterior cells based on the values in the mirror-image interior cells so that the density, pressure, and tangential velocity in the exterior cell agree with those values in the interior while the normal velocity is negated. Then we can simply compute over the extended domain using the algorithm described above, ignoring the boundary. Each wave from the interior which crosses the boundary will be matched by a wave from the exterior in such a way that the normal velocity in mirror-image cells adjacent to the boundary will remain negatives of one another, simulating zero normal velocity on the wall itself.

Alternatively, rather than creating fictitious exterior cells and propagating waves from their interfaces to match interior waves, we can simply reflect the interior waves when they hit the boundary as suggested by Fig. 8.1. If the wave carries increments R_p then the reflected wave carries the same increments of density, pressure, and tangential velocity. The increment of normal velocity is negated.

The latter approach has the advantage that it extends more easily to general boundaries. If the boundary is not flat, creating globally well-defined fictitious cells

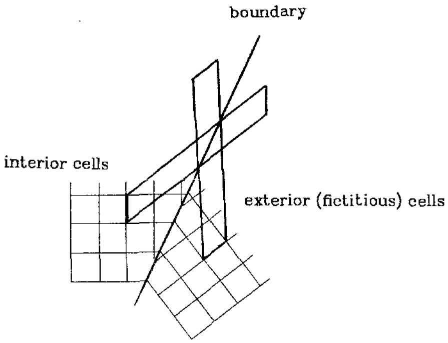

FIG. 8.1. Cartesian mesh cut by a flat boundary. Reflecting the interior cells through this boundary gives the fictitious exterior cells. Each wave propagating across the boundary from an interior cell interface is matched by a wave propagating into the region from a fictitious interface. This can also be viewed as a reflection of the interior wave at the boundary.

by reflecting the interior cells is not possible. It is, however, still possible to reflect waves at the boundary provided only that we assume the boundary is locally flat where it intersects the wave, as can be done to good approximation if the boundary is smooth.

In addition to handling the reflection of waves arising from interior interfaces, it is also necessary to generate a wave from the cell face defining the boundary itself. We solve a one-dimensional Riemann problem normal to the boundary. The left state comes from the interior cell. The right state is the same except that the normal velocity is negated, as motivated by Fig. 8.1 and the previous discussion. Because the two states are related in this manner, the solution of the Riemann problem will give only wave propagating into the computational domain, with zero normal velocity in its wake. Of the other three waves, two will have zero velocity and the third will propagate out of the computational domain and is ignored.

9. Numerical Results

To date the method has been implemented only on a Cartesian grid with "small" time steps, meaning the Courant number is less than one relative to the area h^2 of the regular grid cells. However, boundaries are allowed to cut through this grid and the area of the resulting boundary cells may be arbitrarily small. The boundary is approximated by piecewise linear segments connecting the points where the boundary crosses the grid lines. Consequently all cells are polygons with at most five sides, since we assume each cell contains at most one boundary segment.

Because of the Courant number restriction, wave propagation in the interior cells is easily implemented as discussed in Section 6. It is only near the boundaries that waves may intersect several cells in an unpredictable manner. Each wave is also a polygon which can be represented by a list of its vertices. This polygon can be intersected with the polygonal grid cells and the area of intersection calculated using standard algorithms of computational geometry. A wave that strikes the boundary [illegible] domain which is then reflected through the boundary of the half space to obtain an interior polygon.

This basic algorithm has been fully implemented. The high resolution correction terms have been properly included only at the regular grid cells in the interior. At the boundary an approximation is used that gives reasonable results but can probably be improved upon.

The test cases presented here involve only flat boundaries. The handling of boundary conditions is then equivalent to reflecting the interior cells across the boundary. This minimizes the possible negative effects of the boundary conditions and gives a reasonable test of the basic algorithm in situations where there are irregular small grid cells.

Allowing arbitrarily small boundary cells poses some numerical difficulties not associated with the theoretical stability properties of the method. If the size of a grid cell is on the order of the machine rounding error, then the area of the intersection of that cell with a wave cannot be accurately computed. This can lead to gross errors that will eventually cause noticeable errors in other grid cells and possibly nonphysical flow quantities. In order to avoid such problems, we have chosen to ignore any boundary grid cells with area less than $10^{-2}h^2$. This amounts to introducing imperceptible holes in the otherwise solid boundary. The experiments reported here were performed on a Vaxstation II in single precision.

The first test case is a one-dimensional shock tube problem in a channel at 40 ° to the grid. We take the same initial data as in Section 5. Figure 9.1 shows the boundary cells of the computational grid and contour lines of constant density for the numerical solution at $t=0.3$, using the high resolution method with $h=\frac{1}{40}$ and timestep $k=0.0075$. This gives a Courant number of roughly 0.5 relative to the regular cells, though it is nearly 100 times larger for the smallest irregular cells that are not ignored. Figure 9.1a shows the results obtained with the basic first-order method. Figure 9.1b shows the results when the high resolution correction waves discussed in Section 7 are included. Both figures show contour lines of density as well as the irregular grid cells adjacent to the boundary. Figure 9.2 shows corresponding plots of the density along the lower wall of the channel. Values in each boundary cell are plotted vs distance along the wall. No attempt has been made to extrapolate to the actual boundary location, or to account for the nonuniformity of these boundary cells. Consequently some nonsmoothness is visible in this boundary data (and even more so in Fig. 9.4 below). Plots of grid values down the center of the channel would show much smoother results.

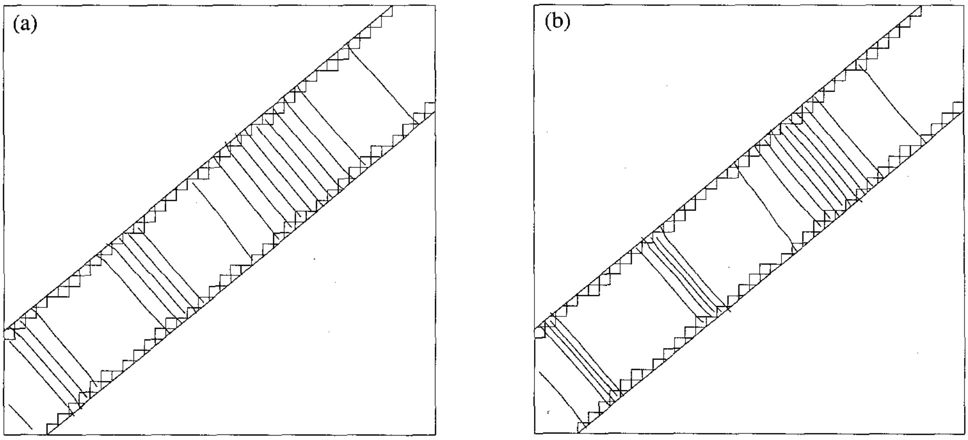

FIG. 9.1. Density contours for a shock tube at 40 ° to the grid. The irregular boundary cells of the computational grid are also shown. (a) First-order method. (b) With high resolution correction waves included.

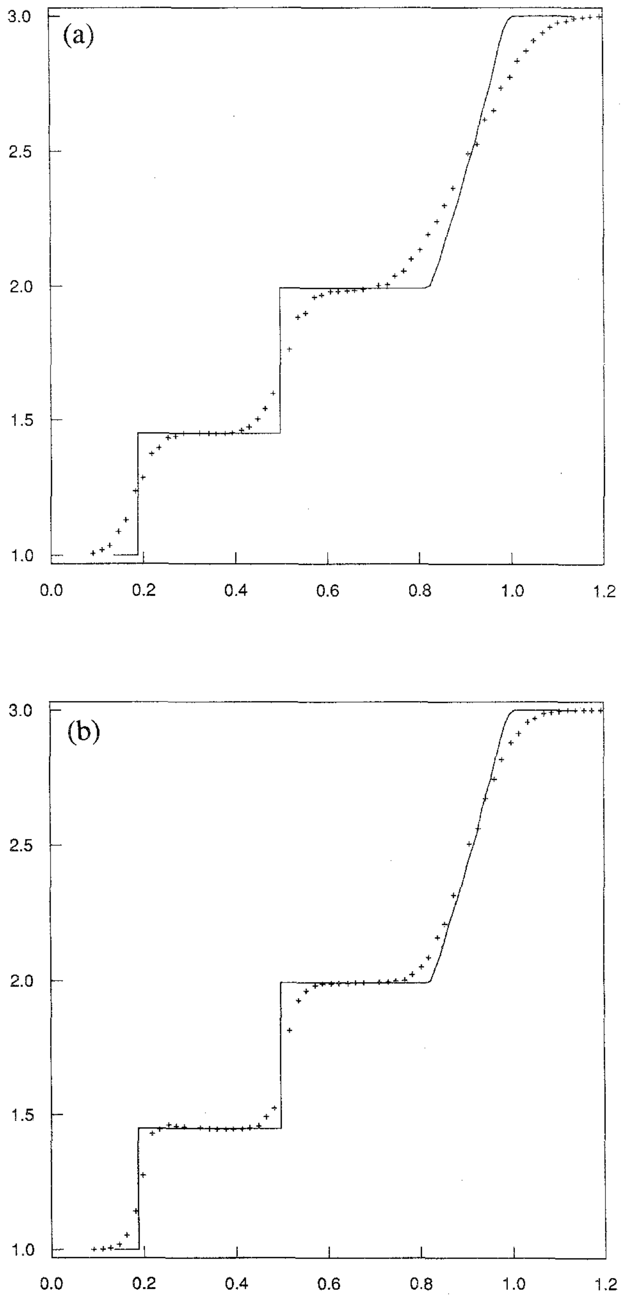

FIG. 9.2. Density in the shock tube along the lower wall. Values in the boundary cells are plotted versus arclength. The solid line is the true solution. (a) First-order method. (b) With high resolution correction waves included.

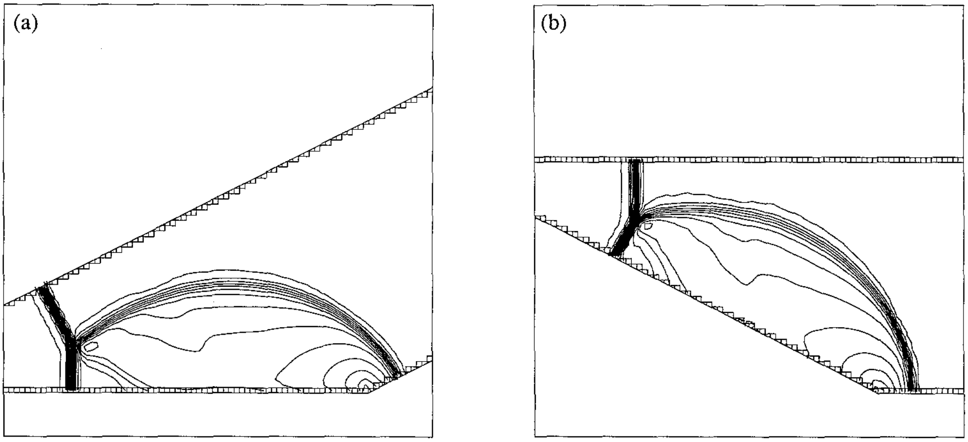

FIG. 9.3. Density contours for Mach 2.03 shock reflection off a 27° ramp. (a) Case I: grid aligned with ramp. (b) Case II: grid aligned with incident shock.

Smearing is clearly reduced by introducing the high resolution correction waves. In both cases the contour plots show that the method is capable of maintaining one-dimensionality of the solution, with essentially the same accuracy in the irregular cells as in the interior. The small boundary cells cause no stability problems.

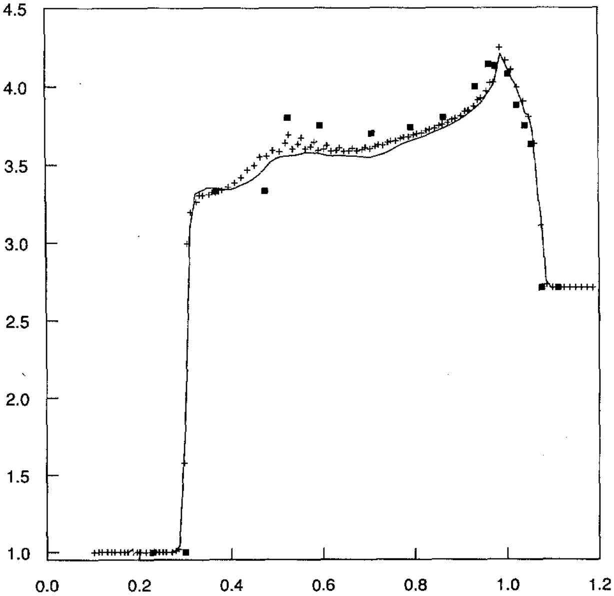

FIG. 9.4. Density along the lower boundary. The solid line shows results from Case I, the + symbols are results from Case II. The squares are experimental results taken from [9].

The second test example is an unsteady shock reflection from a 27° ramp at Mach 2.03, with single Mach reflection. Experimental as well as numerical results for this problem can be found in the paper of Glaz, Collela, Glass, and Deschambault (Case 2 in [9]). The initial flow conditions are $\rho = 0.387$, $v = 0$, $p = 33.3$ ahead of the shock, $\rho = 1.05$, $v = -14.06$, $p = 154.4$ behing the shock, where v if the velocity normal to the shock. The shock was initially distance 0.05 from the ramp corner and results are presented at time 0.275 with $h = \frac{1}{80}$ and $k = 2.5 \times 10^{-4}$ (110 time steps). The results presented here were computed with the high resolution method. Computations with the first-order version have also been done and give the same qualitative results with much more smearing.

For comparison purposes, two different orientations of the ramp are considered. In Case I (Fig. 9.3a), the grid is aligned with the ramp. This is the orientation often used in other codes to avoid irregular grid cells in the region of primary interest (e.g., [9, 29]). In Case II (Fig. 9.3b) the grid is aligned with the incident shock and the ramp cuts through the grid obliquely. In each case 30 equally spaced density contours are plotted. The results agree closely and have essentially the same resolution.

Figure 9.4 shows a plot of relative density (ρ/ρ_0, where $\rho_0 = 0.387$) along the lower wall. The solid line shows the results from Case I while the + symbols show results from Case II. The squares are experimental results taken from [9]. The results are in good agreement and also compare reasonably well with numerical results of [9]. The discontinuities obtained here are not as sharp, particularly the slip line connecting the triple point to the wall. In large part this is due to the coarseness of the grid (essentially 80×40 grid points compared with 350×130 in [9]). Figure 9.4 shows that even in Case II, where the ramp is oblique to the grid, there are at most two points in the shocks.

10. CONCLUSIONS

An approach for deriving high resolution numerical methods has been presented that allows generalization to stable methods on arbitrary grids. Numerical results in two space dimensions show that the accuracy in irregular grid cells is comparable to what is obtained with regular cells. In particular, for Cartesian grids cut by irregular boundaries, it is possible to obtain stable high resolution results with a time step chosen based on the interior regular cells.

Another application of these ideas is to mesh refinement using overlapping rotated Cartesian grids, as in the work of Berger [1, 2]. Again irregular cells are created at the grid interface and the present approach gives a way of deriving conservative interface conditions. This is currently being studied by the author [illegible]

A similar approach toward achieving stability has been taken by Chern and Colella [5]. They give an algorithm for shock tracking across a Cartesian grid in which fluxes are redistributed from small grid cells to neighboring grid cells to ensure stability. Their redistribution procedure is rather ad hoc compared to the wave propagation approach taken here but presumably has the advantage of being much cheaper. A major shortcoming of the present method is its expense. If tangential wave propagation is used in two dimensions, then at each cell interface $m+1$ Riemann problems must be solved and m^2 waves propagated. Even using Roe's approximate Riemann solver (which is easy to vectorize over multiple Riemann problems, particularly on a Cartesian grid), this may be prohibitive for a practical algorithm. On the other hand, it does not seem that so much information should be necessary, and efforts are currently under way to find simplifications of the algorithm by using a smaller number of approximate waves that carry the essential information. One possibility is to use a different kind of wave decomposition in place of the Riemann solutions. Some of the ideas of Roe [24] or Deconinck, Hirsch, and Peuteman [8] might be useful in this regard.

Another practical possibility is to use the algorithm developed here only at irregular boundaries of a Cartesian grid, coupling it to a more efficient standard method in the regular interior cells.

On the other hand, in some applications the approach discussed here may have advantages over standard finite volume or dimensionally split methods even on regular grids. The fact that waves are propagated obliquely to the grid (when tangential propagation is included) may be advantageous in modeling complex two-dimensional phenomena. Tests have shown that including tangential propagation, even when not required for stability, increases the accuracy with which waves oblique to the grid can be tracked.

In some special applications it could also prove useful to use Courant numbers larger than one even on a regular grid. For example, in problems with widely varying wave speeds where the phenomena of primary interest occurs on the slow scale, the fast waves may carry little information but will limit the time step with traditional methods. Using the wave propagation approach allows one to choose a time step appropriate for the slow scale phenomena. This could lead to a simultaneous increase in efficiency and reduction in the numerical dissipation of slow waves.

REFERENCES

1. M. BERGER, Stanford Computer Science Dept. Report STAN-CS-82-924, 1982 (unpublished).
2. M. BERGER AND J. OLIGER, *J. Comput. Phys.* **53**, 484 (1984).
3. J. P. BORIS AND D. L. BOOK, *J. Comput. Phys.* **11**, 38 (1973).
4. Y. BRENIER, *SIAM J. Numer. Anal.* **21**, 1013 (1984).
5. I. L. CHERN AND P. COLELLA, Lawrence Livermore National Laboratory Report UCRL-97200, 1987 (unpublished).
6. D. K. CLARKE, M. D. SALAS, AND H. A. HASSAN, *AIAA J.* **24**, 343 (1986).
7. S. F. DAVIS, ICASE NASA Contractor Report 172179, 1983 (unpublished).
8. H. DECONINCK, C. HIRSCH, AND J. PEUTEMAN, in *10th Int. Conf. on Num. Meth. in Fluid Dyn., Beijing*, 1986.

9. H. M. Glaz, P. Colella, I. I. Glass, and R. L. Deschambault, *Proc. R. Soc. London A* **398**, 117 (1985).
10. J. B. Goodman and R. J. LeVeque, *SIAM J. Numer. Anal.* **25**, 268 (1988).
11. A. Harten, *J. Comput. Phys.* **49**, 357 (1983).
12. A. Harten and J. M. Hyman, *J. Comput. Phys.* **50**, 235 (1983).
13. P. D. Lax, *Hyperbolic Systems of Conservation Laws and the Mathematical Theory of Shock Waves*, SIAM Regional Conference Series in Applied Mathematics Vol. 11 (SIAM, Philadelphia, 1973).
14. R. J. LeVeque, *Commun. Pure Appl. Math.* **37**, 463 (1984).
15. R. J. LeVeque, *SIAM J. Numer. Anal.* **22**, 1051 (1985).
16. R. J. LeVeque, in *Proceedings, 7th Int. Conf. Methods in Appl. Sci. and Eng., Versailles, France*, 1985.
17. R. J. LeVeque, *SIAM J. Numer. Anal.* **25**, 1 (1988).
18. R. J. LeVeque and J. B. Goodman, Lectures in Appl. Math. Vol. 22, p. 51 (Amer. Math. Soc., Providence, RI, 1985).
19. S. Osher and S. Chakravarthy, *SIAM J. Numer. Anal.* **21**, 955 (1984).
20. P. L. Roe, in *Proceedings, Seventh Intl. Conf. on Num. Meth. in Fluid Dynamics*, edited by W. C. Reynolds and R W. MacCormack, Lecture Notes in Physics Vol. 141 (Springer-Verlag, New York/Berlin, 1981).
21. P. L. Roe, *J. Comput. Phys.* **43**, 357 (1981).
22. P. L. Roe, in *Numerical Methods for Fluid Dynamics*, edited by K. W. Morton and M. J. Baines, (Academic Press, New York/London, 1982).
23. P. L. Roe, Lectures in Appl. Math. Vol. 22, p. 163 (Amer. Math. Soc., Providence, RI, 1985).
24. P. L. Roe, ICASE Report 85-18, 1985 (unpublished).
25. P. E. Rubbert *et al.*, in *Computational Mechanics—Advances and Trends*, AMD Vol. 75, edited by A. K. Noor, pp. 49–84, (1986).
26. P. K. Sweby, *SIAM J. Numer. Anal.* **21**, 995 (1984).
27. B. van Leer, *J. Comput. Phys.* **32**, 101 (1979).
28. B. Wedan and J. C. South, AIAA Paper 83-1889-CP, 6th AIAA Computational Fluid Dynamics Conf., 1983.
29. P. Woodward and P. Colella, *J. Comput. Phys.* **54**, 115 (1984).
30. S. T. Zalesak, *J. Comput. Phys.* **31**, 335 (1979).